Certifying Multilevel Coherence in the Motional State of a Trapped Ion

Ollie Corfield,* Jake Lishman,* Chungsun Lee, Jacopo Mosca Toba, George Porter, Johannes M. Heinrich, Simon C. Webster, Florian Mintert, and Richard C. Thompson
Blackett Laboratory, Imperial College London, London SW7 2AZ, United Kingdom
(Dated: June 24, 2021)

Quantum coherence is one of the clearest departures from classical physics, exhibited when a system is in a superposition of different basis states. Here the coherent superposition of three motional Fock states of a single trapped ion is experimentally certified, with a procedure provably robust against imperfect operation. As the motional state cannot be directly interrogated, our scheme uses an interference pattern generated by projective measurement of the coupled qubit state. The minimum number of coherently superposed states is inferred from a series of threshold values based on analysis of the interference pattern. This demonstrates that high-level coherence can be verified and investigated with simple, nonideal control methods well-suited to noisy intermediate-scale quantum devices.

I. INTRODUCTION

A defining feature of quantum mechanics is the ability for a system to be in a coherent superposition of any set of conceivable states. Coherence between states of a natural basis underpins almost all deviation between the predictions of quantum and classical mechanics, however theoretical efforts to rigorously define and quantify it are relatively recent [1–3]. Similar to entanglement, quantum coherence is recognised as a resource [4–6] that may be expended to realise desirable outcomes, such as improving the probability of success in quantum information algorithms [7, 8] and phase-estimation metrology applications [9], the extraction of thermodynamic work [10], or the creation of nonequilibrium entropy [11].

Previous work on coherence metrics has typically focused on producing a quantified value determined by complete reconstruction of the density matrix [5, 12, 13]. In practice, the poor scaling of the number of precise measurements required to perform such state tomography renders it an unattractive prospect beyond small-dimensioned systems. These measures also explore little of the concept of higher-order coherence [4, 14], an analogue of multipartite entanglement, where the quantity of interest is the number of basis states that contribute to a quantum superposition. This multilevel coherence is known to be its own resource within certain quantum information processing operations [6], and is critical to the deeper understanding of quantum transport in regimes of partially coherent dynamics, both in solid-state physics [4] and transport processes on the boundary between coherent and dissipative dynamics [15, 16].

Early efforts to quantify multilevel coherence required the ability to measure in bases that themselves contained some level of coherence [4, 17]. As coherence is defined purely with respect to a basis, usually the only one available for measurements, achieving these schemes experimentally necessitated an extra coherent step. The tested state would undergo several assumed-coherent operations to map the ideal coherent measurement basis onto the actual, typically incoherent, basis of the measurement. Information derived from such experiments would then rely on these operations having been performed accurately. However, these same types of operations form the state creation, which is what is being tested; the operations must be both trusted and tested simultaneously. More recent schemes have sought to avoid these problems by ensuring that their coherence metrics provide a strict lower bound on the amount of higher-order coherence in a state, no matter how successfully intermediate operations were implemented [6]. Of particular interest is the ability to certify this coherence based only on an interference pattern [18], effectively enabling verification of multilevel coherence based on a projective measurement onto only one state. These schemes enable insight into coherence in systems inaccessible by measurement, without risking false positives from imperfect mapping operations. This is of particular interest for noisy intermediate-scale quantum devices, where verification of quantum properties is a laborious task.

Ion traps are a frequently used platform for many quantum technologies, which encode quantum information in two different forms. The coupled motion of co-trapped ions can be cooled into the quantum regime, and used as a means to drive entangling interactions between internal qubit states. However, only the qubit states and not the motion can be measured directly. Trapped ions are well established as media for quantum simulation [19, 20], and high-precision metrology via quantum logic spectroscopy [21, 22]. Additionally they are one of the leading candidates for a full-scale quantum computer [23–26]. Decoherence processes of the motional modes are among the dominant effects reducing quantum logic fidelities, making their classification and understanding imperative. It is possible to fully reconstruct the density matrix and Wigner function of an arbitrary motional state [27], however this requires a large number of measurements.

In this work, we experimentally certify the existence of multiple superposition elements in the motional state of a single trapped ion, using an interference pattern method derived from, and extending, ref. [18]. The only available projective measurement can distinguish the state of the coupled internal-state qubit, but not the different motional states, making it a more general operation than originally considered. We extend the theory by showing that the same method is valid for arbitrary measurement operators. The coherence is defined relative to the physical Fock basis of this motion, where individual elements correspond to different numbers of motional

* These two authors contributed equally.

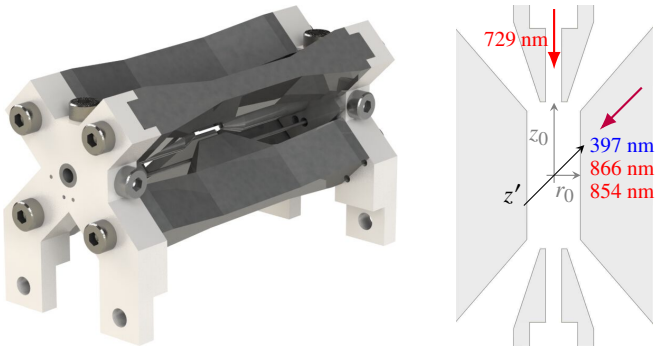

FIG. 1. Linear ion trap (left), based on an Innsbruck-style blade trap design detailed in [28]. The drawing (right) shows a cross section through the electrodes. The trap dimensions are $z_0 = 2.75\,\text{mm}$ and $r_0 = 1\,\text{mm}$. Also shown is the interaction geometry between lasers and the magnetic field quantisation axis, labelled z'.

quanta. Further, we show that this coherence can be created and verified using only the simplest operations in trapped ions on a noisy device.

II. IMPLEMENTATION

The system Hamiltonian of a single two-level ion in a harmonic trap, considering only a single motional mode with annihilation operator $\hat{a}$, is

$$\hat{\mathcal{H}}/h = \frac{1}{2}\nu_{eg}\hat{\sigma}_z + \nu_m\hat{a}^\dagger\hat{a}. \tag{1}$$

Here, ν_{eg} is the frequency separation of two qubit states $|g\rangle$ and $|e\rangle$, and ν_m the trap frequency, which gives the uniform separation of oscillator Fock states $|n\rangle$ representing physical quanta of motion in the system. In principle the motional states can contain arbitrarily high levels of coherence, making them ideal candidates for investigation, though hampered by the lack of direct measurement available. The experimental aim is to create arbitrary superpositions of different Fock states in the motion, and certify their multilevel coherence properties using only simple operations and measurements of the qubit.

A. Trap

A linear rf trap confines particles radially with an oscillating quadrupole electric field [29], and a three dimensional harmonic potential is realised with the addition of a static axial potential [30]. The electrode structure of the trap used in the following experiments is detailed in fig. 1. As only a single oscillator is required, the axial mode is used with frequency $\nu_m \approx 1.1\,\text{MHz}$. The radial field, though not directly relevant here, provides tighter confinement ($\approx 1.85\,\text{MHz}$).

The qubit is mapped onto the $S_{1/2,m_j=1/2} \leftrightarrow D_{5/2,m_j=1/2}$ quadrupole transition in $^{40}Ca^+$ at 729 nm. This π-transition is least sensitive to noise in the magnetic field of 0.393 mT, in the direction of the quantisation field, z'. Coherent population transfer between the qubit states is driven by a laser–quadrupole interaction tuned to the qubit frequency, $\nu_{eg} \approx 411\,\text{THz}$. The coupling strength of this interaction is termed the Rabi frequency Ω. The transition is driven by a diode laser locked to an external cavity to achieve a linewidth below 1 kHz. The laser frequency and amplitude are controlled by an acousto-optic modulator driven by an arbitrary waveform generator. The laser is directed through a hole in the axial electrodes in order for the wavevector k to only project onto the axial motion. This gives a Lamb–Dicke parameter for the system of $\eta = k\sqrt{\hbar/(4\pi m\nu_m)} \approx 0.09$, where m is the mass of the ion.

Dipole transitions at 397 nm and 866 nm are used in Doppler cooling, with the emitted fluorescence monitored by a photomultiplier tube. These lasers are also utilised in measurement of the qubit state via electron shelving, as they do not couple to the excited level. Readout fidelity is obtained from the overlap of bright and dark photon-count distributions, and is reliably above 99%. A third dipole transition at 854 nm is addressed in order to pump any excited-state population back to the ground state to initialise each experiment.

B. Sideband Pulses

Population transfer between different motional levels is driven by interactions detuned from the qubit frequency ν_{eg} by multiples of the motional frequency ν_m. Inside the Lamb–Dicke regime of weak qubit–motion coupling, there are three available processes which drive transitions between the two qubit states: the carrier that leaves the motion unchanged, and the red (blue) sideband that removes (adds) a phonon of motion when exciting the qubit state. Each operation is parametrised by two variables: the time the driving is applied for, and the phase shift of the laser relative to the initial operation. The Rabi frequencies of these interactions are dependent on the number of phonons and the oscillations of different pairs are generally not coperiodic. In the Lamb–Dicke regime, Rabi frequencies of the red and blue sidebands are given by $\eta\Omega\sqrt{n}$ and $\eta\Omega\sqrt{n+1}$, respectively.

While the red or blue sidebands are being driven, the nearby stronger carrier transition causes undesired off-resonant effects that reduce the fidelity of sideband operations. The two dominant manifestations of this are: the AC Stark effect shifting the resonance frequency of the sideband, causing imperfect population transfer and the accumulation of phase errors; and fast small-amplitude oscillations between the qubit states close to the trap frequency, which are being driven on the carrier and are not necessarily nulled on completion of the pulse. The frequency shift is mitigated by applying a concurrent compensation pulse detuned far from all resonances on the opposite side of the carrier from the target sideband, with its exact frequency and driving strength calibrated such that the net AC Stark shift is zero. This compensation drive does, however, contribute further to the off-resonant excitation of the carrier.

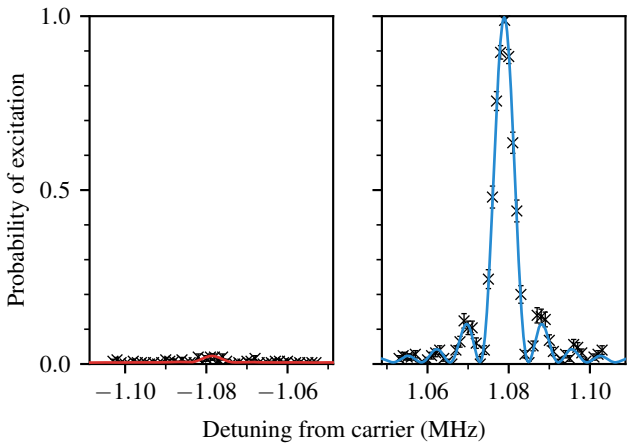

FIG. 2. Ground state cooled excitation spectrum of first-order red (left) and blue (right) sidebands. The fitted model gives a mean thermal occupation of $\bar{n} = 0.02(2)$. The fit also includes the carrier, which is not shown here for clarity.

C. State Preparation

From the perspective of the coherence certification, the creation of the state to test is a black box operation. Since this experiment is self-contained, though, it is first necessary to construct several states to be investigated. After Doppler cooling, the motion of the ion is approximated by a thermal distribution with $\bar{n} \approx 10$. The ion is initialised in the $|g,0\rangle$ state by sideband cooling. The probability of success is 98(2)%, determined from the excitation spectrum in fig. 2.

The method used here to create motional superpositions is an extension to previous work that can synthesise any joint qubit–motion state in a single trapped ion [31, 32], taking advantage of how the $|g,0\rangle$ ($|e,0\rangle$) state is unaffected by the red (blue) sideband, and is illustrated in fig. 3. Considering the operation in reverse and starting from the target state, the motional excitation is gradually stepped downwards either directly by a sideband pulse, or by combining two populations so that the next step may continue the descent. At the end, the adjoint of the sequence is taken to produce the forwards operation.

This algorithm produces an infinite but discrete family of solutions, and it is possible to find the sequence with minimal duration. Whenever the carrier is used, the population can be combined into either $|g\rangle$ or $|e\rangle$ as in fig. 3c, and there are an infinite number of pulse lengths that will achieve the desired population transfer at every step. Sideband Rabi oscillations between higher motional states are faster than between lower states, but these pulses are calculated first. It may be advantageous to choose a longer early pulse or prefer combining population in one qubit state over the other, in order to realise time gains in the slower parts of the sequence. After an initial candidate solution is found by arbitrarily resolving the choices, the best solution can be found by restarting the algorithm and recursively trying every path while pruning solutions that become too long.

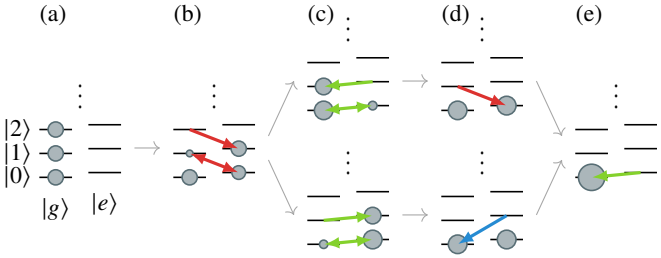

FIG. 3. The algorithm used to produce arbitrary motional superpositions [31], illustrated creating $\big(|g,0\rangle + |g,1\rangle + |g,2\rangle\big)/\sqrt{3}$. Grey circles represent superposition state occupation with size proportional to population, while green, red and blue arrows represent carrier, red and blue sideband transitions respectively. (a) Consider the system beginning in the target state. (b) A red-sideband pulse is applied to move all of the highest-occupied motional state $|2\rangle$ into the state with one quantum of motion fewer; this affects all other states by different amounts that must be tracked. (c) The now-highest-occupied motional state $|1\rangle$ has population in both qubit states, so the carrier is used to combine both into either $|g,1\rangle$ or $|e,1\rangle$. (d) Depending on the previous pulse, the red or blue sideband is used to reduce the highest motional state again, combining populations in $|g,1\rangle$ and $|e,0\rangle$ (red), or $|e,1\rangle$ and $|g,0\rangle$ (blue), into the motional ground state. (e) A final carrier combines the population into $|g,0\rangle$. The desired forwards operation is simply the adjoint of the derived sequence.

III. COHERENCE CERTIFIER

The coherence of a system is defined with respect to a particular basis. The eigenstates of the system Hamiltonian are a natural choice, typically having a clear physical interpretation, and are often the only readily accessible measurement basis. A pure state $|\psi\rangle = \sum_j \zeta_j |j\rangle$ is commonly called k-coherent in a basis $\{|j\rangle\}$ if there are at least k nonzero coefficients ζ_j. A mixed state ρ is then k-coherent if for all possible pure-state decompositions $\rho = \sum_i q_i |\psi_i\rangle\langle\psi_i|$, there is at least one k-coherent element $|\psi_i\rangle$ with a nonzero probability q_i. This is similar to equivalent definitions used when classifying entanglement [33]. These definitions produce a discrete hierarchy for coherence.

The purpose of a coherence metric is to have a single number, measurable by a simple experiment, that imparts some information on the coherence level of the given state. Coherence can be certified with such a figure of merit if, for each level of coherence, there is a theoretically maximal value achievable, and these maximal values are strictly increasing with increasing levels of coherence. The maximal values then form a series of thresholds: measuring a value greater than the largest achievable from any k-coherent state unambiguously implies that the state was at least $(k+1)$-coherent. The specific observable metric must also be impervious to errors in any intermediate operations or direct measurements made; the procedure will typically require coherent manipulation, and deviations from the intended scheme must not cause the certifier value to increase beyond a threshold it would not otherwise achieve. A certifier satisfying these constraints will not necessarily identify all states coherent at a certain level, but will never produce a false positive for higher-order coherence; it

can certify the existence of multilevel coherence, but not prove its absence.

A. Interference-Pattern Methods

To be most useful, a certifier must be achievable with few, easily accessible measurements. Interference patterns are a basic tool for verifying quantum coherence between two states. Any evidence of oscillatory behaviour in the well known Ramsey experiment on a quantum system is sufficient to verify 2-coherence. It is desirable to continue in this vein; interference patterns are a function of only one control parameter and are produced by simple projective measurements onto one basis state, so are easily experimentally achievable.

The particular interference patterns considered here are higher-order extensions of the Ramsey experiment. An input state ρ to be tested for coherence undergoes free evolution of a controlled duration, either by waiting an amount of time or phase-shifting the control fields, before a predetermined pulse sequence is applied to map the coherent basis of interest back to the measurement basis. The dynamics of this measurement with varying time or phase determine the interference pattern. Here, as the system under consideration is a harmonic oscillator, the free-evolution dynamics $\hat{\mathcal{U}}_\mathrm{f}$ are periodic, so the time parameter can be replaced by the phase ϕ of this period. Explicitly, the interference pattern is

$$p(\phi) = \langle\chi|\,\hat{\mathcal{U}}_\mathrm{m}\hat{\mathcal{U}}_\mathrm{f}(\phi)\rho\,\hat{\mathcal{U}}_\mathrm{f}^\dagger(\phi)\hat{\mathcal{U}}_\mathrm{m}^\dagger\,|\chi\rangle \tag{2}$$

where $\hat{\mathcal{U}}_\mathrm{m}$ is the operation mapping the coherent basis to the measurement basis, and $|\chi\rangle$ is the basis state whose population is measured. In the special case of the two-state Ramsey sequence, an optimal measurement mapping is the adjoint of the operation used to create the initial superposition.

The certifier C used here is a function of normalised moments

$$M_n = \frac{1}{2\pi}\int_0^{2\pi} p(\phi)^n\,d\phi, \tag{3}$$

of this interference pattern. No single moment is suitable taken alone, however the ratio

$$C = \frac{M_3}{M_1^2}, \tag{4}$$

satisfies the requisites [18]. It requires the pattern to be evaluated at only a few different free-evolution phases for good statistics, as it relies only on low-order moments. Obtaining a value of C greater than 1 requires 2-coherence, greater than $5/4 = 1.25$ requires 3-coherence, and greater than $179/96 \approx 1.86$ is necessary to certify 4-coherence in a Hilbert space of arbitrary dimension [18]. While the metric can certify the presence of coherence, this threshold system does not provide the completely tight bounds needed to unambiguously certify the *absence* of coherence above a given level. For example, any 3-coherent state can exhibit a value of C lower than the $5/4$ threshold if the state distinguishability is low or if the measurement-mapping operation is implemented poorly.

B. General Measurements

This coherence metric is resilient in the face of imperfect realisation of coherent operations during the measurement-mapping procedure, however the analysis of ref. [18] is valid only when the actual measurement is a projection onto a single basis state. In order to be used for coupled systems, it must first be shown that the same hierarchical structure of the threshold values applies for general measurements. This can be demonstrated by showing that the thresholds for determining certain levels of coherence remain the same, regardless of the type of measurement.

The interference pattern in eq. (2) is generalised to

$$p(\phi) = \mathrm{Tr}\big[\hat{\mathcal{A}}\hat{\mathcal{U}}_\mathrm{m}\hat{\mathcal{U}}_\mathrm{f}(\phi)\rho\,\hat{\mathcal{U}}_\mathrm{f}^\dagger(\phi)\hat{\mathcal{U}}_\mathrm{m}^\dagger\big], \tag{5}$$

where $\hat{\mathcal{A}}$ is an element of a positive operator-valued measure (POVM). Projections onto a single basis state are rank-1 matrices with $\hat{\mathcal{A}} = |\chi\rangle\langle\chi|$, for a measurement-basis state $|\chi\rangle$. The only measurement available in the ion trap is a projective measurement on the qubit state only, such as $\hat{\mathcal{A}} = |g\rangle\langle g|\otimes\hat{\mathbb{I}}_\mathrm{mot}$, where $\hat{\mathbb{I}}_\mathrm{mot}$ is the identity operator on the motional space. This is a type of higher-rank projective measurement, but the proof is applicable to general measurements.

As in ref. [18], the analysis is performed in terms of a harmonic oscillator with eigenstates $\{|n\rangle\}$. Any periodic free-evolution can be modelled as such by inserting non-interacting states with the otherwise-absent intermediate energy levels. This includes Hilbert spaces with tensor-product structure, as in trapped ions, by relabelling the states with a single index n. Using the decompositions $\rho = \sum_{n,m}\rho_{nm}\,|n\rangle\langle m|$ and $\hat{\mathcal{A}} = \sum_{n,m}A_{nm}\,|n\rangle\langle m|$, the interference pattern can be written as

$$p(\phi) = \sum_n \rho_{nn}A_{nn} + 2\sum_{n>m}|\rho_{mn}A_{nm}|\cos\big((n-m)\phi+\theta_{nm}\big), \tag{6}$$

where θ_{nm} is the complex phase of $\rho_{mn}A_{nm}$.

In this form, the value of the first moment of the interference pattern M_1 is the sum of the ϕ-independent terms. The only nonzero terms of the moment M_3 are each proportional to $\cos(\theta_{n_1,m_1}\pm\theta_{n_2,m_2}\pm\cdots)$, so the certifier C will reach a maximal value when all the θ are zero, and ρ and $\hat{\mathcal{A}}$ can be taken as real-symmetric matrices without loss of generality in determining threshold values.

The maximum achievable value of C for a 2-coherent state under these general measurements can be verified analytically. To be less than 3-coherent, ρ may have at most two nonzero diagonal elements in the coherence basis, and one upper-triangular off-diagonal entry. The value of C is not dependent on particular energy levels, so for simplicity these are labelled 0 and 1. The convexity of C is unaffected by the general measurement, so it is sufficient to consider only pure states. The state can be parametrised by a real value $0 \le x \le 1$ as $\sqrt{x}\,|0\rangle + \sqrt{1-x}\,|1\rangle$. The value of the certifier is then

$$C = xA_{00} + (1-x)A_{11} + \frac{6x(1-x)A_{01}^2}{xA_{00}+(1-x)A_{11}}. \tag{7}$$

In order for the measurement operator to be a valid POVM value, the two diagonal elements must individually be between

0 and 1, and the off-diagonal element must satisfy

$$A_{01} \leq \min\Big\{A_{00}A_{11},\, (1-A_{00})(1-A_{11})\Big\}. \tag{8}$$

It is clear that if x, A_{00} or A_{11} are either 0 or 1 exactly, this is equivalent to the incoherent case, and the maximum value of C is 1. Further, C is always maximised by maximising the magnitude of the off-diagonal element A_{01}, and so only the equality in eq. (8) need be considered. The two branches of the minimum correspond to using $\hat{\mathcal{A}}$ or $1-\hat{\mathcal{A}}$ as the measurement, so without loss of generality it is possible to consider only $A_{01} = A_{00}A_{11}$ and $A_{00} + A_{11} \leq 1$.

The maximal value of C can be found from eq. (7), using the method of Lagrangian multipliers with the constraints $0 < \{x, A_{00}, A_{11}\} < 1$ and $A_{00} + A_{11} \leq 1$. Only the latter bound can be tight, so the Lagrangian can be written as

$$\mathcal{L} = C - \lambda(A_{00} + A_{11} - 1), \tag{9}$$

with $\lambda \geq 0$. The derivative with respect to A_{00} is

$$\frac{\partial \mathcal{L}}{\partial A_{00}} = x\frac{x^2A_{00}^2 + 2x(1-x)A_{00}A_{11} + 7(1-x)^2A_{11}^2}{\big[xA_{00} + (1-x)A_{11}\big]^2} - \lambda, \tag{10}$$

and the derivative with respect to A_{11} is the same under the transformations $x \to 1-x$ and $A_{00} \leftrightarrow A_{11}$. Under the constraints, the fraction is strictly greater than zero, so when also satisfying the complementary slackness condition $\lambda(A_{00} + A_{11} - 1) = 0$, the stationary points of the Lagrangian all have $A_{11} = 1 - A_{00}$. With this, the optimal measurement operator can be written in the $\{|0\rangle, |1\rangle\}$ basis as

$$\hat{\mathcal{A}} = \begin{pmatrix} A_{00} & \sqrt{A_{00}(1-A_{00})} \\ \sqrt{A_{00}(1-A_{00})} & 1-A_{00} \end{pmatrix}, \tag{11}$$

or similarly in the full coherence basis with padding zeros in all other positions. This is exactly the form of a rank-1 projective measurement on the state $\sqrt{A_{00}}\,|0\rangle + \sqrt{1-A_{00}}\,|1\rangle$, and consequently the maximal value of C obtainable with a general measurement on a 2-coherent state remains $5/4$, using the proofs given in ref. [18]. It is therefore sufficient to observe a value of C greater than $5/4$ to certify that the underlying state is at least 3-coherent, no matter the type of measurement used. Numerical optimisations are strongly suggestive that the thresholds remain the same for all orders of multilevel coherence.

C. Measurement-Mapping Sequences

While the certifier cannot produce false positives, it is still necessary to attempt to apply a suitable measurement-mapping sequence in order to maximise the chance of a conclusive result. The motional states whose coherence is being tested cannot be measured directly in the trapped-ion system in any basis; the only available measurement distinguishes the two qubit states. The measurement-mapping sequence can be chosen to effectively convert this high-rank projective measurement into a rank-1 projective measurement, which can be constructed to produce optimal patterns.

The given state is first tested to determine which motional levels are occupied, and to verify that only one qubit state has population. The latter can be achieved by a direct projective measurement of the qubit state. The motional populations are then measured by a Rabi-type experiment; the blue sideband is applied for a varying amount of time, followed by a projective measurement on the qubit. This produces an oscillatory pattern, shown in fig. 4, that verifies the populations of the motional states, but neither involves nor verifies any coherence between the different motional levels; the same pattern will be found if the state is completely mixed, or if the motional levels have any relative phases between them. The relative populations of the motional states can be estimated from this data, as each undergoes oscillation at a separate but known frequency, approximately proportional to $\sqrt{n+1}$ for small numbers of phonons n.

An efficient measurement-mapping sequence can be realised if the target motional state is mapped onto one of the two qubit states, and all orthogonal states are mapping onto the other qubit state. In the standard two-state Ramsey experiment the target state is $(|g,0\rangle + |g,1\rangle)/\sqrt{2}$, and a measurement mapping that is the inverse of the simplest creation protocol generates the required behaviour. This simple inversion is insufficient in general, however, as the adjoint of the creation operation does not necessarily map states that are orthogonal to the target into the other qubit state.

For a target state with a maximum occupied phonon number n, there are initially $2n+2$ elements of the system basis that need to be considered when creating the mapping. However, as the previous tests determine which basis elements have nonzero probability, all $n+1$ of the $|e\rangle$ states may be ignored, as well as any unoccupied phonon states in $|g\rangle$. This still generally requires mapping several motional states to one qubit state. As an example, the measurement mapping $\hat{\mathcal{U}}_{\mathrm{m}}$ for a target state $(|g,0\rangle + |g,1\rangle + |g,2\rangle)/\sqrt{3}$ should satisfy

$$\begin{aligned} \hat{\mathcal{U}}_{\mathrm{m}}\big(|g,0\rangle + |g,1\rangle + |g,2\rangle\big) &\propto |e,\lambda_1\rangle\,, \\ \hat{\mathcal{U}}_{\mathrm{m}}\big(|g,0\rangle - 2\,|g,1\rangle + |g,2\rangle\big) &\propto |g,\lambda_2\rangle\,, \text{ and} \\ \hat{\mathcal{U}}_{\mathrm{m}}\big(|g,0\rangle - |g,2\rangle\big) &\propto |g,\lambda_3\rangle\,, \end{aligned} \tag{12}$$

where the motional states $\{|\lambda_i\rangle\}$ may be chosen freely, as they have no effect on the measurement and are only necessary to keep the mapping operation unitary. The other states on the left-hand side of eq. (12) can similarly be chosen arbitrarily, provided they complete a basis of the space of populated system states. Since these are the eigenstates of phase evolution, no additional states can become populated during the wait period. The aim of tailoring a measurement-mapping operation for each state is to maximise the visibility of the interference pattern. Any certifier is valid for any state within the same populated subspace, however a poorly designed map will generally produce inconclusive tests.

A sequence of sideband pulses producing dynamics satisfying eq. (12) was found for each target state presented here. The error in such a map is the total probability that a measurement taken after the map is applied to one of the states in

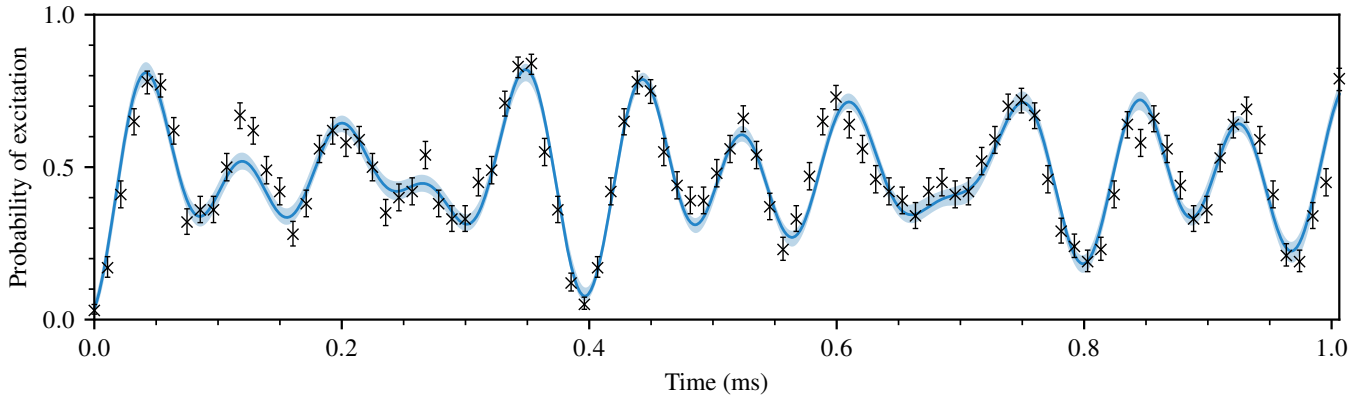

FIG. 4. Time evolution of state $\big(|g,0\rangle + |g,1\rangle + |g,2\rangle\big)/\sqrt{3}$, while driving the blue-sideband transition. The data points (black crosses) are the measured excitation probabilities with Wilson binomial 1-σ confidence bounds indicated by error bars. The best fit (darker blue line) was found by maximum-likelihood estimation, and the 95% confidence region (lighter blue shaded region) was found by bootstrapping the measured data 14 000 times. The fit was made over the sideband Rabi frequency, sideband detuning, motional dephasing rate, and a reduced density matrix including correlations only between directly coupled elements. The Rabi frequency coupling the $|g,0\rangle$ state was estimated at 6.94(3) kHz, with oscillation from $|g,n\rangle$ increased by a factor of $\sqrt{n+1}$. The populations in $|g,0\rangle$, $|g,1\rangle$ and $|g,2\rangle$ were 33(2)%, 30(2)% and 33(2)%, respectively, with 4.7(14)% outside the desired basis elements, where the errors denote the 1-σ confidence region from bootstrapping. These values all have significant negative covariance, as expected. All appreciable undesired population was in the $|e\rangle$ excited qubit state; the motional state $|3\rangle$ was included in the fit, but found to have a population consistent with zero with a standard error of 9×10^{-3} percentage points.

	State creation				Measurement mapping				
Transition	carrier	red	carrier	red	red	carrier	red	carrier	red
Pulse length	0.50	0.70	0.73	0.71	0.71	0.50	1.42	1.59	0.72
Phase offset $/\pi$	0	−0.50	1.00	0.50	0	0.71	−0.29	0.10	−0.51

TABLE I. Pulse sequence for creation and measurement mapping of target state $\big(|g,0\rangle + |g,1\rangle + |g,2\rangle\big)/\sqrt{3}$. Only carrier and red sideband transitions are used. The pulse length is scaled relative to the oscillation frequency of the coupled pair that includes the motional $|0\rangle$ state, so that a value of 1 is the time taken to exchange $|g,0\rangle \leftrightarrow |e,0\rangle$ on the carrier and $|g,1\rangle \leftrightarrow |e,0\rangle$ on the red sideband. The given phase is applied as an offset, so that the set laser phase at the beginning of a pulse is offset relative to where it would have been had it oscillated freely at its transition frequency since the beginning of the experiment. The interference pattern is constructed by adding a varying phase offset on the red-sideband pulses during the measurement mapping.

eq. (12) would not produce the desired value. The sequences were found by numerical minimisation of this error over the duration and phase of each pulse in a variety of candidate sequences. In practice, many sequences exist that result in a probability consistent with zero to a tolerance of 10^{-10}, usually by alternating a motion-modifying sideband with the carrier. The sequences used here do not increase the total motional excitation considered by the system. The first pulse is typically the inverse of the last step of the corresponding creation sequence, reducing the highest-occupied phonon state by one. All subsequent red- and blue-sideband pulses except the last are then a single period of the dynamics of this greatest coupled motional pair with varying phases, so the phonon count never rises above its initial maximum, though the interspersed carrier pulses may be of any duration.

The particular sequence of pulses used to create the target state $\big(|g,0\rangle + |g,1\rangle + |g,2\rangle\big)/\sqrt{3}$ is shown in table I, along with the subsequent measurement-mapping sequence. The specifications of sequences for other states are presented in Appendix A, and in machine-readable format in the Supplemental Information [35]. For the example target state, the simulated (line) and experimentally realised (points) dynamics are shown in fig. 5. This depicts how the population of the qubit $|e\rangle$ state varies over the duration of the sequence, with no phase evolution. The fast oscillations caused by the off-resonant carrier excitation are clearly visible during sideband pulses in simulations, with a second distinct frequency component as a result of the Stark-shift compensation pulse.

To produce the interference pattern, a period of phase evolution $\hat{\mathcal{U}}_\mathrm{f}(\phi)$ under the system Hamiltonian eq. (1) must be implemented. In any reference frame, this evolution manifests itself as a phase offset to the applied laser field producing the interactions; one interpretation is that the laser phase advancement is paused while it is not interacting with the ion. In practice one can apply an arbitrary phase offset to the laser field, allowing any free-evolution phase-accumulation to be applied in constant time. When applying a free-evolution phase of ϕ, all following red-sideband pulses are phase-shifted by $-\phi$, while all blue-sideband pulses are offset by ϕ, and the carrier is untouched. This free-evolution period is imposed between the state creation and measurement-mapping sequences, so only the final five pulses in table I and fig. 5 are affected, for exam-

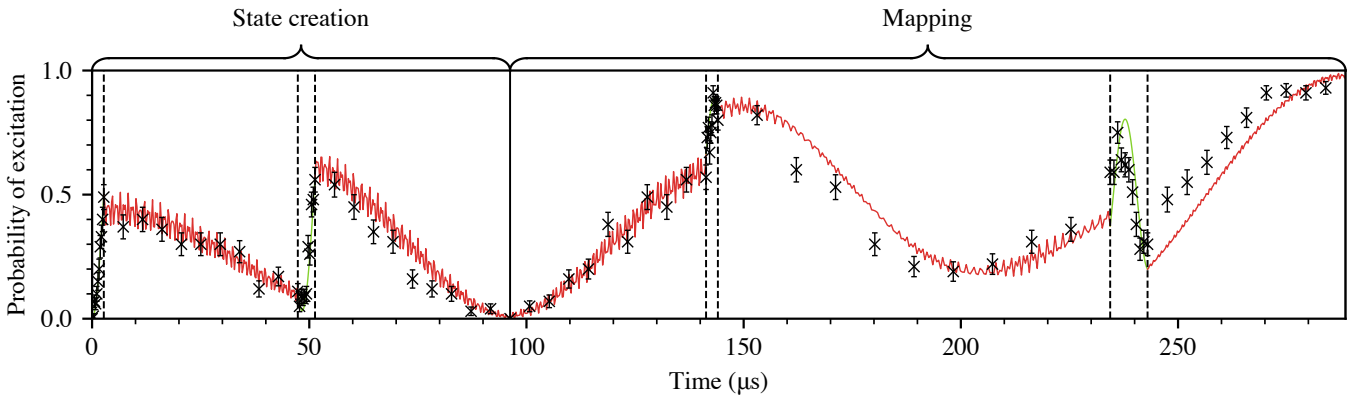

FIG. 5. Probability of excitation of the qubit state during the experiment outlined in table I. The data (crosses) are shown compared to a numerical simulation (lines) made with QuTiP [34] using the best estimators of the trap parameters determined during calibration. The time taken to transfer population between the ground and excited states on the carrier transition is 5.4 μs. With no phase evolution applied, $\phi = 0$, the qubit should be fully excited on completion of the measurement-mapping sequence. However, the accumulation of phase errors from imperfect realisation of the pulses leads to an increasing discrepancy between data and model, predominantly caused by frequency mis-sets, and dephasing of the qubit.

ple. This is the same operation as pausing the laser evolution, except for time-dependent noise processes which are relevant to determining the duration for which coherence remains, but not to the certification of its initial presence.

IV. EXPERIMENTAL RESULTS

The two-element superposition state $(|g,1\rangle + |g,2\rangle)/\sqrt{2}$ was used to initially demonstrate the procedures for preparation and coherence certification of arbitrary motional states. This state was chosen as it is the lowest-excitation two-element superposition state that requires basis-element populations to interact coherently during the creation, and that does not give a full-visibility interference pattern when the mapping operation is the inverse of the creation. For an idealised realisation of this state, this naïve choice of measurement-mapping sequence can only produce an interference pattern with a theoretical maximum peak-to-peak visibility of ≈ 0.88. Instead, the more rigorous measurement-mapping sequences described in section III C were used to give the full-visibility pattern seen in fig. 6(a). The value of C of 1.090(12) is, as expected, less than the 3-coherence threshold of $5/4 = 1.25$, which no 2-coherent state can exceed. After preparing the state using the method of section II C, the populations of $|g,1\rangle$ and $|g,2\rangle$ were estimated to be 54.7(14)% and 38.0(13)%, respectively, with 7.2(16)% outside these targeted basis elements. These population numbers and associated 1-σ confidence bounds were found by maximum-likelihood estimation using the blue-sideband-probe technique. The population outside the desired basis elements caused the visibility of the measured interference pattern to be slightly reduced, which, along with other imperfections in implementation, prevented the derived value of C from reaching its maximal value.

Evidence of any oscillation is sufficient to certify 2-coherence, allowing verification even with poor choices of measurement-mapping sequences. This is not the case for higher-order coherence. For the state $(|g,0\rangle + |g,1\rangle + |g,2\rangle)/\sqrt{3}$, if the mapping is again the inverse of the state-creation sequence, the certifier has a theoretical maximal value of $C \approx 0.92$. This is significantly below the threshold to certify 3-coherence, in part because the peak-to-peak visibility of the pattern could not exceed ≈ 0.68. Instead, the optimised measurement mapping specified in table I was used, with the resulting interference pattern shown in fig. 6(b). This gave a measured value of $C = 1.54(2)$, above the threshold of 1.25, unequivocally certifying the state as 3-coherent in the motional basis. The maximal value, produced with perfect creation and measurement mapping, is $47/27 \approx 1.74$. This particular measurement illustrates the robustness of the metric to imperfect measurement-mapping operations. Immediately after state preparation, the populations in the three targeted basis elements $|g,0\rangle$, $|g,1\rangle$ and $|g,2\rangle$ were 33(2)%, 30(2)% and 33(2)%, respectively, and 4.7(14)% was outside this basis. These values were derived from the data in fig. 4. All of the missing population appeared in the excited qubit state $|e\rangle$ rather than higher motional states, consistent with numerical simulations of the creation sequence with experimental defects, suggesting that most imperfections entered during the longer mapping sequence. In addition, the solid grey numerical-simulation curve in fig. 6(b) is not statistically consistent with the measured data at the 1-σ level, suggesting that other, unaccounted for, imperfections were present during the mapping operation. Despite these demonstrable errors, the certifier C is known to be unable to produce false-positives [18], and the presence of 3-coherence can therefore be trusted.

It is to be expected that higher orders of coherence are more difficult to create and certify. Figure 6(c) shows the interference pattern resulting from the attempted creation and measurement of an equal, in-phase 4-element superposition of $|g,0\rangle$ through $|g,3\rangle$. The measured interference-pattern data only achieved $C = 1.35(3)$, below the 4-coherence threshold

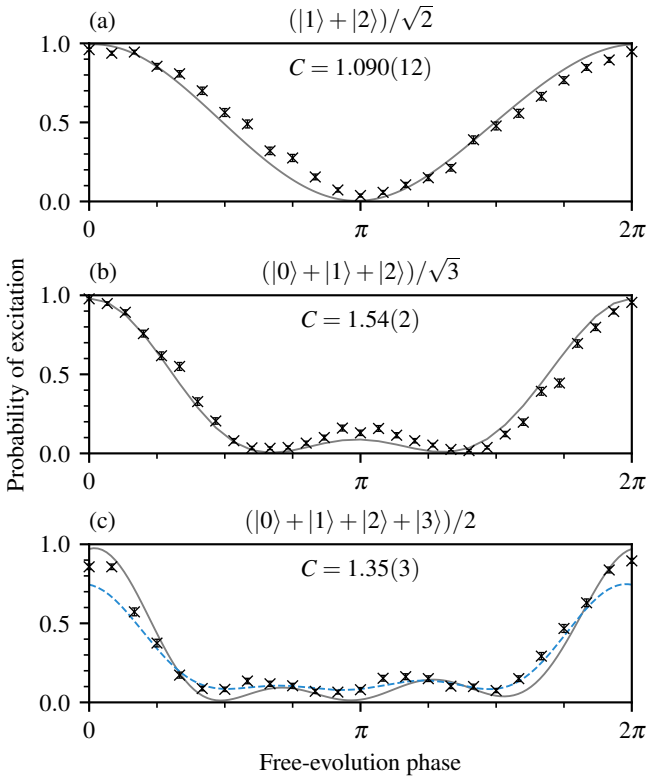

FIG. 6. Measured interference patterns (black crosses) for the motional states indicated, using the full measurement-mapping sequences calculated to give a theoretically maximal pattern visibility. The models (solid grey line) are numerical simulations using experimental parameter values measured during the trap calibration. In all cases, the target also has the qubit in the ground $|g\rangle$ state. The typical Rabi frequency on the carrier was 90 kHz, and 400 shots were taken per plotted data point. The depicted probability errors are from the standard estimators of binomial distributions, and are mostly contained within the drawn points. The values of C and their uncertainties are determined through numerical integration of the moments of the patterns, with statistical corrections to account for estimator bias. (a): the value of C is greater than the threshold needed to unambiguously certify 2-coherence, although the clear oscillation would be a sufficient indicator regardless. (b): the value of C, 1.54(2), is sufficient to verify that the created state had least three coherent superposition elements. (c): the created state was intended to be 4-coherent, however the value of $C = 1.35(3)$ is only great enough to verify a 3-coherent state. The blue dashed line is a pattern from the 3-coherent state that best approximates the data while matching the known state populations from the blue-sideband scan, found numerically. The unconvincing fit suggests that the underlying state may well have been 4-coherent, even though the C-test was inconclusive.

of $179/96 \approx 1.86$. This is an inconclusive result; it is possible that the state was 4-coherent immediately after creation, but imperfections in the mapping meant that this went unverified. The populations of the four basis elements were 29(2)%, 25(2)%, 21(2)% and 22(2)%, respectively, with 3.7(14)% outside the expected-state subspace. The nature of the creation sequences requires some degree of coherence to be present in order to achieve such population numbers, offering evidence in support of this hypothesis. To further illustrate this key point, the dashed blue line in fig. 6(c) is a simulated interference pattern resulting from the same mapping, implemented perfectly, applied to a 3-coherent motional state consistent with the estimated populations. The state was chosen to maximise the likelihood of measuring the given data, yet the resulting fit is not very convincing. This mismatch to the measured pattern shape is also suggestive that the underlying state was, in fact, 4-coherent, but a sufficient build-up of imperfections led to the moment ratio C being less than the certification threshold. If one is prepared to relax the tolerance for certification from "beyond reasonable doubt" to a model-dependent "balance of probability", this maximum-likelihood estimation extends the analysis without additional experimental cost. Exceeding a threshold with C still, however, meets the former standard of proof, as was the case for the certification of 3-coherence in both this and the previous states.

V. DISCUSSION

In moving from a theoretical description of the coherence certifier to a physical realisation, it is important to recognise the potential violations of assumptions, to ensure that the fail-safe nature of the metric is not contravened. Imperfections in realising the mapping operation $\hat{\mathcal{U}}_{\mathrm{m}}$ cannot result in measuring a value of C in excess of the relevant threshold for any input state, provided that such imperfections are independent of the free-evolution phase ϕ [18]. It is worth considering how such a phase-dependent error might enter during the experiment, in order to be confident that no such effect has impacted the measurements. To illustrate with an extreme example, an incoherent state $|0\rangle$ could be incorrectly measured as 2-coherent if the implemented mapping created a projection on to an evolution-phase-dependent state $\cos\phi\,|0\rangle + \sin\phi\,|1\rangle$, or the state-distinction measurement had a time-dependent accuracy.

The particular method of effecting the free-evolution period by applying phase shifts to the laser fields eliminated several classes of time-dependent error. With no physical wait time, the duration of every shot of a given interference pattern was equal, preventing time-dependent drifts in controls from introducing extra features to the patterns. The free-evolution phase shifts were all added by the arbitrary waveform generator as part of the same procedure as fixing the phase of a sideband pulse in sequence, and consequently any error is independent of the magnitude of the intended shift. All other time-dependent variations were addressed by randomising the order in which the data points were taken. Each data point depicted in fig. 6 was derived from 400 individual shots. To create a pattern, four rasters through each set of free-evolution phases were taken, each providing 100 shots to every point, with the order of the phases randomised for each raster. Approximately, this converts any possible periodic drifts into incoherent white-noise processes spread evenly across the measurements.

While these particular steps severely limit the possibility of drift artificially inflating the measured value of the certifier, they do not affect systematic miscalibrations of the various transition frequencies. Severe but stable deviations from the

two sideband frequencies could, in principle, lead to a phase dependence of the measurement mapping. These could arise either from imperfect compensation of the AC Stark effect, or from systematic mis-sets of the laser frequencies. The most noticeable effects of detuning from a sideband by an amount δ are a modification of the sideband Rabi frequency Ω' and a reduction in Rabi-flop visibility, both by a factor of $\sqrt{1+\delta^2/\Omega'^2}$. This timing error results in the free-evolution phase-advancement operations applying two different erroneous phases to the sidebands, producing an incorrect mapping operation that depends on the amount of phase to be applied.

This can be detected principally by observing sideband probes similar to fig. 4 taken immediately after ground-state cooling with less-than-unity visibility. Frequency fluctuation measurements in the trap suggested deviations in the sideband calibration frequency were less than $\delta/\Omega' = 0.15$ over the course of one experimental run. However, the time-dependent components of this drift were converted to incoherent processes by the aforementioned point randomisation, which in simulations completely dominated any remnant effects that might have overestimated the value of C. Similarly, any possible contributions from the small-amplitude high-frequency oscillations stemming from the nearby carrier transition are rendered incoherent by the drift of the relevant parameters, and consequently cannot cause C to increase beyond a threshold.

A final consideration is the effect of incomplete statistics on the estimator of C. The individual shots of data making up the interference pattern are samples from independent Bernoulli distributions, and the estimator $\hat{C}$ and its uncertainty must be derived from these. A naïve estimator constructed by a direct discretisation of the integrals in the definition of the moments leads to

$$\hat{C}_{\text{naïve}} = \frac{\sum_i w_i(\bar{p}_i)^3}{\left(\sum_i w_i \bar{p}_i\right)^2}, \tag{13}$$

for numerical integration weights $\{w_i\}$ and excited-state probability estimators $\{\bar{p}_i\}$. The integration weights chosen are predetermined, and depend only on the quadrature method to be used and the locations of the sampled free-evolution phases. However, the nonlinear dependence of this estimator on the $\bar{p}_i$ results in it having a systematic bias upwards; for perfect observations of a state that achieves a threshold value of C, the estimated value $\hat{C}_{\text{naïve}}$ would be more likely than not to produce a value that was too high, and this increase would not be accounted for by a simple lowest-order propagation of uncertainty. Instead, the estimator of C and its standard deviation used in this work are derived from eq. (13) with additional bias-correction terms calculated from the method of moments [36] using estimators of the binomial distribution's central moments up to and including the skewness [37]. At 400 shots-per-point, any remaining bias was found by Monte-Carlo simulation to be at an order of magnitude smaller than the quoted uncertainties. Full details of the statistical estimators used are presented in Appendix B.

VI. CONCLUSION

Multilevel coherence can be unambiguously certified by interference-pattern experiments varying a single parameter, even in cases where the physical system of interest is not accessible to direct measurement. These methods only require an available measurement on any coupled system, and are robust against imperfections in the implementation of coherent manipulations mapping the target system to the measurement basis. With the exception of poor measurement statistics, they cannot produce a false positive. Even in cases where the certification test is inconclusive at a particular level, additional maximum-likelihood estimation can be used to indicate whether it is probable that this degree of coherence was achieved, still based only on the interference pattern.

The motion of a single trapped ion can be controlled using only first-order sideband pulses to create nonclassical states that exhibit multilevel coherence. This can be unambiguously verified by measurements made only of the associated qubit system, similarly using only first-order coupling transitions. The simplicity of these required operations demonstrate the applicability of the coherence-certification method to any physical system where some elements are slow, unreliable or unfeasible to measure. This includes any set of entangled qudits where some of the systems may not be accessed by interrogation fields, such as in cavity optomechanics or superconducting qubits coupled to a resonator.

Verification of the entanglement and coherence properties of arbitrary quantum states is experimentally taxing, often needing full reconstruction of the density operator. This requires a level of control beyond current noisy intermediate-scale quantum devices. The problem is exacerbated when some subsystems are inaccessible to measurement, subjecting tomographic procedures to large errors, and they are rendered completely unreliable when coherent manipulations of the system cannot be trusted. The resilient interference-pattern metrics presented here do not suffer such limitations. The certification is read from a simple, single statistic of a data set found by varying a single parameter, and is consequently far more forgiving of statistical uncertainty than those based on decompositions of a matrix where each element has a large confidence interval.

Despite decoherence being a major roadblock to large-scale quantum computing, the intricacies of high-order coherence remain little understood. The uses of coherence as a resource are also still being actively investigated for their roles in thermodynamic and solid-state transport processes. These interference-pattern metrics provide an experimentally realistic method to effect these analyses, paving the way to a greater understanding of the fundamental nature of quantum mechanics.

ACKNOWLEDGMENTS

We are immensely grateful to Brian Willey for his role in the fabrication of the trap and other laboratory equipment. Financial support by EPSRC through all of *Optimal control for robust ion trap quantum logic* Grant No.

EP/P024890/1, *Hub in Quantum Computing and Simulation* Grant No. EP/T001062/1, the *Centre for Doctoral Training in Controlled Quantum Dynamics* Grant No. EP/L016524/1, and the *Training and Skills Hub in Quantum Systems Engineering* Grant No. EP/P510257/1 is gratefully acknowledged.

	State creation				Measurement mapping				
Transition	carrier	red	carrier	red	red	carrier	red	carrier	red
Pulse length	0.60	0.80	0.74	0.71	0.71	0.44	1.41	0.54	1.41
Phase offset $/\pi$	0	−0.50	0	−0.50	0	−0.66	−0.83	−0.87	−0.41

TABLE II. Pulse sequences for creation and measurement mapping of target state $\big(|g,1\rangle + |g,2\rangle\big)/\sqrt{2}$.

	State creation				Measurement mapping				
Transition	carrier	red	carrier	red	red	carrier	red	carrier	red
Pulse length	0.50	0.70	0.73	0.71	0.71	0.50	1.42	1.59	0.72
Phase offset $/\pi$	0	−0.50	1.00	0.50	0	0.71	−0.29	0.10	−0.51

TABLE III. Pulse sequences for creation and measurement mapping of target state $\big(|g,0\rangle + |g,1\rangle + |g,2\rangle\big)/\sqrt{3}$.

	State creation						Measurement mapping								
Transition	carrier	red	carrier	red	carrier	red	red	carrier	blue	carrier	red	carrier	red	carrier	red
Pulse length	0.51	0.55	0.96	0.57	0.84	0.58	2.89	1.47	1.15	3.02	2.31	4.69	2.31	0.72	0.58
Phase offset $/\pi$	0	−0.50	−1.00	0.50	0	−0.50	0	−0.16	−0.41	−0.53	0.45	0.79	−0.32	−0.13	0.76

TABLE IV. Pulse sequences for creation and measurement mapping of target state $\big(|g,0\rangle + |g,1\rangle + |g,2\rangle + |g,3\rangle\big)/2$.

Appendix A: Pulse Sequence for all States

This appendix tabulates the pulse sequences used for the state creation and measurement mapping for each of the states presented in the main text, in tables II to IV. The pulse length is scaled relative to the oscillation frequency of the coupled pair that includes the motional $|0\rangle$ state, so that a value of 1 is the time taken to exchange $|g,0\rangle \leftrightarrow |e,0\rangle$ on the carrier and $|g,1\rangle \leftrightarrow |e,0\rangle$ on the red sideband. The given phase is applied as an offset, so that the set laser phase at the beginning of a pulse is offset relative to where it would have been had it oscillated freely at its transition frequency since the beginning of the experiment. The interference pattern is constructed by varying the phase offsets of all blue- and red-sideband pulses during the measurement mapping sequences only. The phase offset should be added to blue-sideband pulses, and subtracted from red-sideband pulses.

Appendix B: Statistics of the Moment Ratio

1. Estimating the Moment Ratio

Each point of an interference pattern is an independent binomial distribution with some exact underlying probability μ_j, which is estimated by taking a number of shots n and counting the number of "successes". The estimates p_j are unbiased estimates of the means of the distributions. The quantity of interest is

$$\bar{c} = \frac{m_3}{m_1^2} = \frac{\frac{1}{2\pi}\int_0^{2\pi} p(\phi)^3\, d\phi}{\left(\frac{1}{2\pi}\int_0^{2\pi} p(\phi)\, d\phi\right)^2}, \tag{B1}$$

using a finite number of points (J, the number of p_j) and a finite number of shots. The interference patterns vary sufficiently smoothly that the trapezium rule is appropriate, so

$$\frac{1}{2\pi}\int_0^{2\pi} f(x)\, dx \approx \sum_{j=0}^{J-1} w_j f\Big(\frac{2\pi j}{J-1}\Big), \quad \text{where } w_j = \begin{cases} \frac{1}{2(J-1)} & j = 0 \text{ or } j = J-1 \\ \frac{1}{J-1} & \text{all other } j. \end{cases} \tag{B2}$$

Let $P_j \sim \mathrm{B}(n,\mu_j)/n$ be the distribution from which each of the p_j estimates are drawn. Similarly, let

$$C \sim \frac{\sum_j w_j P_j^3}{\left(\sum_j w_j P_j\right)^2} \tag{B3}$$

be the distribution of the estimates c of the true value $\bar{C}$.

The expectation of a measurement of C is $\mathrm{E}[C]$ where the expectation runs over all the independent probability distributions P_j. For each point's distribution the expectation is $\mathrm{E}[P_j] = \mathrm{E}\big[\mu_j + (P_j - \mu_j)\big]$. The unusual form is to permit a Taylor expansion of the expectation of C around the binomial means in terms of $\mathrm{E}\big[(P_j - \mu_j)^n\big]$, the central moments of the distributions. For the binomial distribution, unbiased estimators (symbols with hats) of these are:

$$\begin{aligned}
\mathrm{E}\big[(P_j - \mu_j)^1\big] &\to p_j - \hat{\mu}_j = 0 && \text{(mean)} \\
\mathrm{E}\big[(P_j - \mu_j)^2\big] &\to \hat{\sigma}_j^2 \quad = \frac{p_j(1-p_j)}{n-1} && \text{(variance)} \\
\mathrm{E}\big[(P_j - \mu_j)^3\big] &\to \hat{\kappa}_j \quad = \frac{p_j(1-p_j)(1-2p_j)}{(n-1)(n-2)} && \text{(skewness).}
\end{aligned} \tag{B4}$$

The expansion, up to terms of third order, is

$$\begin{aligned}
\mathrm{E}[C] &= \mathrm{E}\left[\Big(\sum_j w_j P_j^3\Big)\Big(\sum_j w_j P_j\Big)^{-2}\right] \\
&\approx \frac{\tilde{m}_3}{\tilde{m}_1^2} + \underbrace{\frac{1}{\tilde{m}_1^2}\sum_j\left(3w_j\Big(\mu_j - \frac{2}{\tilde{m}_1}\mu_j^2 + \frac{\tilde{m}_3}{\tilde{m}_1^2}\Big)\mathrm{E}\big[(P_j-\mu_j)^2\big] + w_j\Big(1 - \frac{6}{\tilde{m}_1^2}w_j\mu_j + \frac{9}{\tilde{m}_1^2}w_j^2\mu_j^2 - 4\frac{\tilde{m}_3}{\tilde{m}_1^3}w_j^2\Big)\mathrm{E}\big[(P_j-\mu_j)^3\big]\right)}_{\text{bias term}},
\end{aligned} \tag{B5}$$

where $\tilde{m}_1 = \sum_j w_j\mu_j$ and $\tilde{m}_3 = \sum_j w_j\mu_j^3$. The desired estimator is $\hat{c} = \tilde{m}_3/\tilde{m}_1^2$, so to make a fair estimator the bias term in eq. (B5) must be subtracted from the "direct" measurement c.

2. Estimating Variance

The variance is well approximated in this case by the low-order expansion

$$\sigma_c \approx \sqrt{\sum_j \left|\frac{\partial\hat{c}}{\partial p_j}\right|^2 \sigma_{p_j}^2}\,, \tag{B6}$$

as direct measurements (c) of C are approximately normally distributed, and there is no covariance between the p_j. The estimator $\hat{c} = c - \sum_j z_{2j} - \sum_j z_{3j}$, where z_{nj} is the term in eq. (B5) including $\mathrm{E}\big[(P_j-\mu_j)^n\big]$. The derivatives are then

$$\begin{aligned}
\frac{\partial z_{2k}}{\partial p_j} &= \frac{p_k(1-p_k)}{n-1}\left(\frac{8w_jw_k^2p_k^2}{\tilde{m}_1^4} + \frac{9w_jw_k^2p_j^2}{\tilde{m}_1^4} - \frac{6w_jw_kp_k}{\tilde{m}_1^3} - \frac{12w_jw_k^2\tilde{m}_3}{\tilde{m}_1^5}\right) \\
&\quad + \delta_{jk}\left[\frac{p_k(1-p_k)}{n-1}\left(\frac{3w_k}{\tilde{m}_1^2} - \frac{12w_k^2p_k}{\tilde{m}_1^3}\right) + \frac{1-2p_k}{n-1}\cdot\frac{3w_k}{\tilde{m}_1^2}\left(p_k - \frac{2w_kp_k^2}{\tilde{m}_1} + \frac{\tilde{m}_3w_k}{\tilde{m}_1^2}\right)\right]
\end{aligned} \tag{B7}$$

for the second-order correction terms, and

$$\begin{aligned}
\frac{\partial z_{3k}}{\partial p_j} &= \frac{p_k(1-p_k)(1-2p_k)w_j}{(n-1)(n-2)}\left(-\frac{2w_k}{\tilde{m}_1^3} + \frac{20\tilde{m}_3w_k^3}{\tilde{m}_1^6} + \frac{24w_k^2p_k}{\tilde{m}_1^4} - \frac{36w_k^3p_k^2}{\tilde{m}_1^5} - \frac{12w_k^3p_j^2}{\tilde{m}_1^3}\right) \\
&\quad + \delta_{jk}\frac{w_k}{\tilde{m}_1^2}\left[\left(\frac{18w_k^2p_k}{\tilde{m}_1^2} - \frac{6w_k}{\tilde{m}_1^2}\right)\frac{p_k(1-p_k)(1-2p_k)}{(n-1)(n-2)} + \left(1 - \frac{6w_kp_k}{\tilde{m}_1^2} + \frac{9w_k^2p_k^2}{\tilde{m}_1^2} - \frac{4\tilde{m}_3w_k^2}{\tilde{m}_1^3}\right)\frac{6p_k^2-6p_k+1}{(n-1)(n-2)}\right]
\end{aligned} \tag{B8}$$

for the third-order corrections.

3. Validity of Estimators

Figure 7 shows Monte-Carlo approximations to the probability density functions of the two unbiased and naïve estimators (crosses) and Gaussian approximations of these distributions, using a 31-point trapezium rule and 100 shots-per-point for an

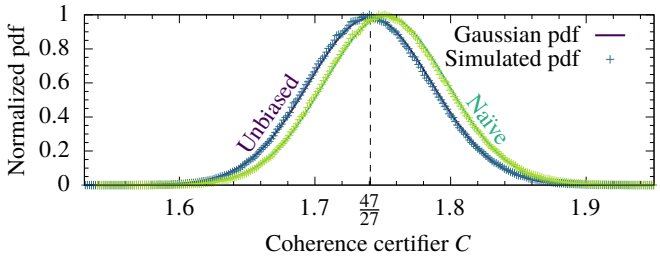

FIG. 7. Normalised probability density functions for the unbiased and biased estimators of the true value $\bar{c}$ using a 31-point trapezium rule with 100 shots-per-point. The plots show direct interpolations of the pdfs (crosses) overlaid on Gaussian approximations (solid lines). The Gaussian approximation is excellent, though a very minor skewness is detectable in the direct interpolations. The probability distributions were approximated by binning the measured values from one million simulations of measurement of a pattern whose analytic moment ratio $C = 47/27$. Each data point in each simulation was found by randomly sampling a binomial distribution with 100 shots at the expected probability. The same data sets were used to evaluate both estimators. The naïve estimator even with 100 shots per point systematically overestimates the true value, whereas the unbiased one is correct.

idealised superposition state $\big(|0\rangle + |1\rangle + |2\rangle\big)/\sqrt{3}$ There is a small skewness visible in the Monte-Carlo pdfs, which shows the true distribution of c is not exactly Gaussian, though this is a very minor effect. The plot shows the bias in the naïve estimator clearly; an unbiased estimator should have a mean at $47/27$ as marked by the dashed vertical line.

[1] D. K. L. Oi and J. Åberg, Physical Review Letters **97**, 220404 (2006), arXiv:0603157 [quant-ph].
[2] D. Girolami, Physical Review Letters **113**, 170401 (2014), arXiv:1403.2446.
[3] A. Streltsov, G. Adesso, and M. B. Plenio, Reviews of Modern Physics **89**, 041003 (2017).
[4] F. Levi and F. Mintert, New Journal of Physics **16**, 033007 (2014).
[5] T. Baumgratz, M. Cramer, and M. B. Plenio, Physical Review Letters **113**, 140401 (2014), arXiv:1311.0275.
[6] M. Ringbauer, T. R. Bromley, M. Cianciaruso, L. Lami, W. Y. S. Lau, G. Adesso, A. G. White, A. Fedrizzi, and M. Piani, Physical Review X **8**, 041007 (2018), arXiv:1707.05282.
[7] M. Hillery, Physical Review A **93**, 012111 (2016).
[8] H.-L. Shi, S.-Y. Liu, X.-H. Wang, W.-L. Yang, Z.-Y. Yang, and H. Fan, Physical Review A **95**, 032307 (2017), arXiv:1610.08656.
[9] A. Castellini, R. Lo Franco, L. Lami, A. Winter, G. Adesso, and G. Compagno, Physical Review A **100**, 012308 (2019), arXiv:1903.10582.
[10] K. Korzekwa, M. Lostaglio, J. Oppenheim, and D. Jennings, New Journal of Physics **18**, 023045 (2016), arXiv:1506.07875.
[11] J. P. Santos, L. C. Céleri, G. T. Landi, and M. Paternostro, npj Quantum Information **5**, 23 (2019), arXiv:1707.08946.
[12] A. Winter and D. Yang, Physical Review Letters **116**, 120404 (2016), arXiv:1506.07975.
[13] X. Yuan, H. Zhou, Z. Cao, and X. Ma, Physical Review A **92**, 022124 (2015), arXiv:1505.04032.
[14] J. Sperling and W. Vogel, Physica Scripta **90**, 074024 (2015), arXiv:1004.1944.
[15] N. Lambert, Y.-N. Chen, Y.-C. Cheng, C.-M. Li, G.-Y. Chen, and F. Nori, Nature Physics **9**, 10 (2013).
[16] J. Cao, R. J. Cogdell, D. F. Coker, H.-G. Duan, J. Hauer, U. Kleinekathöfer, T. L. C. Jansen, T. Mančal, R. J. D. Miller, J. P. Ogilvie, V. I. Prokhorenko, T. Renger, H.-S. Tan, R. Tempelaar, M. Thorwart, E. Thyrhaug, S. Westenhoff, and D. Zigmantas, Science Advances **6**, eaaz4888 (2020).
[17] K. von Prillwitz, Ł. Rudnicki, and F. Mintert, Physical Review A **92**, 052114 (2015), arXiv:1409.1814.
[18] B. Dive, N. Koukoulekidis, S. Mousafeiris, and F. Mintert, Physical Review Research **2**, 013220 (2020), arXiv:1901.08599.
[19] R. Blatt and C. F. Roos, Nature Physics **8**, 277 (2012), arXiv:0905.0118.
[20] B. P. Lanyon, C. Hempel, D. Nigg, M. Muller, R. Gerritsma, F. Zahringer, P. Schindler, J. T. Barreiro, M. Rambach, G. Kirchmair, M. Hennrich, P. Zoller, R. Blatt, and C. F. Roos, Science **334**, 57 (2011).
[21] P. O. Schmidt, T. Rosenband, C. Langer, W. M. Itano, J. C. Bergquist, and D. J. Wineland, Science **309**, 749 (2005).
[22] T. Rosenband, P. Schmidt, D. Hume, W. Itano, T. Fortier, J. Stalnaker, K. Kim, S. Diddams, J. Koelemeij, J. Bergquist, and D. Wineland, Physical Review Letters **98**, 220801 (2007).
[23] C. Monroe, R. Raussendorf, A. Ruthven, K. R. Brown, P. Maunz, L.-M. Duan, and J. Kim, Physical Review A **89**, 022317 (2014).
[24] C. D. Bruzewicz, J. Chiaverini, R. McConnell, and J. M. Sage, Applied Physics Reviews **6**, 021314 (2019), arXiv:1904.04178.
[25] C. J. Ballance, T. P. Harty, N. M. Linke, M. A. Sepiol, and D. M. Lucas, Physical Review Letters **117**, 060504 (2016), arXiv:1512.04600.
[26] J. P. Gaebler, T. R. Tan, Y. Lin, Y. Wan, R. Bowler, A. C. Keith, S. Glancy, K. Coakley, E. Knill, D. Leibfried, and D. J. Wineland, Physical Review Letters **117**, 060505 (2016), arXiv:1604.00032.
[27] D. Leibfried, D. M. Meekhof, B. E. King, C. Monroe, W. M. Itano, and D. J. Wineland, Phys. Rev. Lett. **77**, 4281 (1996).
[28] S. Gulde, *Experimental Realisation of Quantum Gates and the Deutsch-Jozsa Algorithm with Trapped* $^{40}Ca^{+}$ *Ions*, Ph.D. thesis, Universität Innsbruck (2003).
[29] W. Paul, Reviews of Modern Physics **62**, 531 (1990).
[30] D. Leibfried, R. Blatt, C. Monroe, and D. J. Wineland, Review

of Modern Physics **75**, 281 (2003).
[31] S. A. Gardiner, J. I. Cirac, and P. Zoller, Physical Review A **55**, 1683 (1997).
[32] A. Ben-Kish, B. DeMarco, V. Meyer, M. Rowe, J. Britton, W. M. Itano, B. M. Jelenković, C. Langer, D. Leibfried, T. Rosenband, and D. J. Wineland, Physical Review Letters **90**, 037902 (2003).
[33] S. Szalay, Phys. Rev. A **92**, 042329 (2015).
[34] J. Johansson, P. Nation, and F. Nori, Computer Physics Communications **184**, 1234 (2013).
[35] See Supplemental Information at https://github.com/ImperialCQD/Certifying-Multilevel-Coherence-in-the-Motional-State-of-a-Trapped-Ion.
[36] G. Casella and R. L. Berger, *Statistical inference*, 2nd ed. (Thomson Learning, 2002).
[37] L. H. Chan, K. Chen, C. Li, C. W. Wong, and C. Y. Yau, Journal of Statistical Computation and Simulation **90**, 747 (2020).